ADVANCED MATERIALS
www.advmat.de

Overcoming Energy-Scaling Barriers: Efficient Ammonia Electrosynthesis on High-Entropy Alloy Catalysts

*Di Yin, Bowen Li, Boxiang Gao, Mengxue Chen, Dong Chen, You Meng, Shuai Zhang, Chenxu Zhang, Quan Quan, Lijie Chen, Cheng Yang, Chun-Yuen Wong, and Johnny Chung Yin Ho**

Electrochemically converting nitrate (NO_3^-) to value-added ammonia (NH_3) is a complex process involving an eight-electron transfer and numerous intermediates, presenting a significant challenge for optimization. A multi-elemental synergy strategy to regulate the local electronic structure at the atomic level is proposed, creating a broad adsorption energy landscape in high-entropy alloy (HEA) catalysts. This approach enables optimal adsorption and desorption of various intermediates, effectively overcoming energy-scaling limitations for efficient NH_3 electrosynthesis. The HEA catalyst achieved a high Faradaic efficiency of 94.5 ± 4.3% and a yield rate of 10.2 ± 0.5 mg h^{-1} mg_{cat}^{-1}. It also demonstrated remarkable stability over 250 h in an integrated three-chamber device, coupling electrocatalysis with an ammonia recovery unit for continuous NH_3 collection. This work elucidates the catalytic mechanisms of multi-functional HEA systems and offers new perspectives for optimizing multi-step reactions by circumventing adsorption-energy scaling limitations.

1. Introduction

Nitrate (NO_3^-), a widespread contaminant in polluted groundwater and industrial wastewater, presents a promising nitrogen source for sustainable ammonia (NH_3) electrosynthesis.[1,2] However, the multi-step NO_3^--to-NH_3 conversion faces significant challenges. The activity is limited by a volcano-shaped dependency on the key intermediate in the rate-determining step, as the adsorption energies of multiple intermediates on the same active site are linearly correlated.[3–5] Consequently, the practical application of the nitrate reduction reaction (NO_3RR) is hampered by high kinetic barriers and substantial energy consumption, primarily due to the difficulty in avoiding adsorption-energy scaling relations.[6,7]

Interestingly, a survey of the correlation between binding energies of reactants and catalytic activity reveals that a broad binding energy distribution can enhance the ability to tailor traditional scaling relations in cascade reactions (**Figure 1**).[8] Bifunctional catalytic materials with coupled active sites have been explored as tandem systems to modulate binding energy.[9–11] However, these tandem catalysts often

D. Yin, B. Li, B. Gao, D. Chen, Y. Meng, S. Zhang, C. Zhang, Q. Quan, J. C. Y. Ho
Department of Materials Science and Engineering
City University of Hong Kong
Hong Kong, SAR 999077, P. R. China
E-mail: johnnyho@cityu.edu.hk

M. Chen, C.-Y. Wong
Department of Chemistry
City University of Hong Kong
Hong Kong, SAR 999077, P. R. China

Y. Meng, J. C. Y. Ho
State Key Laboratory of Terahertz and Millimeter Waves
City University of Hong Kong
Hong Kong, SAR 999077, P. R. China

C. Zhang
State Key Laboratory of Radio Frequency Heterogeneous Integration (Shenzhen University)
College of Electronics and Information Engineering
Shenzhen 518060, P. R. China

L. Chen
CIMC Offshore Co., Ltd.
Shenzhen 518000, P. R. China

C. Yang
Institute of Materials Research
Tsinghua Shenzhen International Graduate School
Shenzhen 518055, P. R. China

J. C. Y. Ho
Institute for Materials Chemistry and Engineering
Kyushu University
Fukuoka 816 8580, Japan

The ORCID identification number(s) for the author(s) of this article can be found under https://doi.org/10.1002/adma.202415739

DOI: 10.1002/adma.202415739

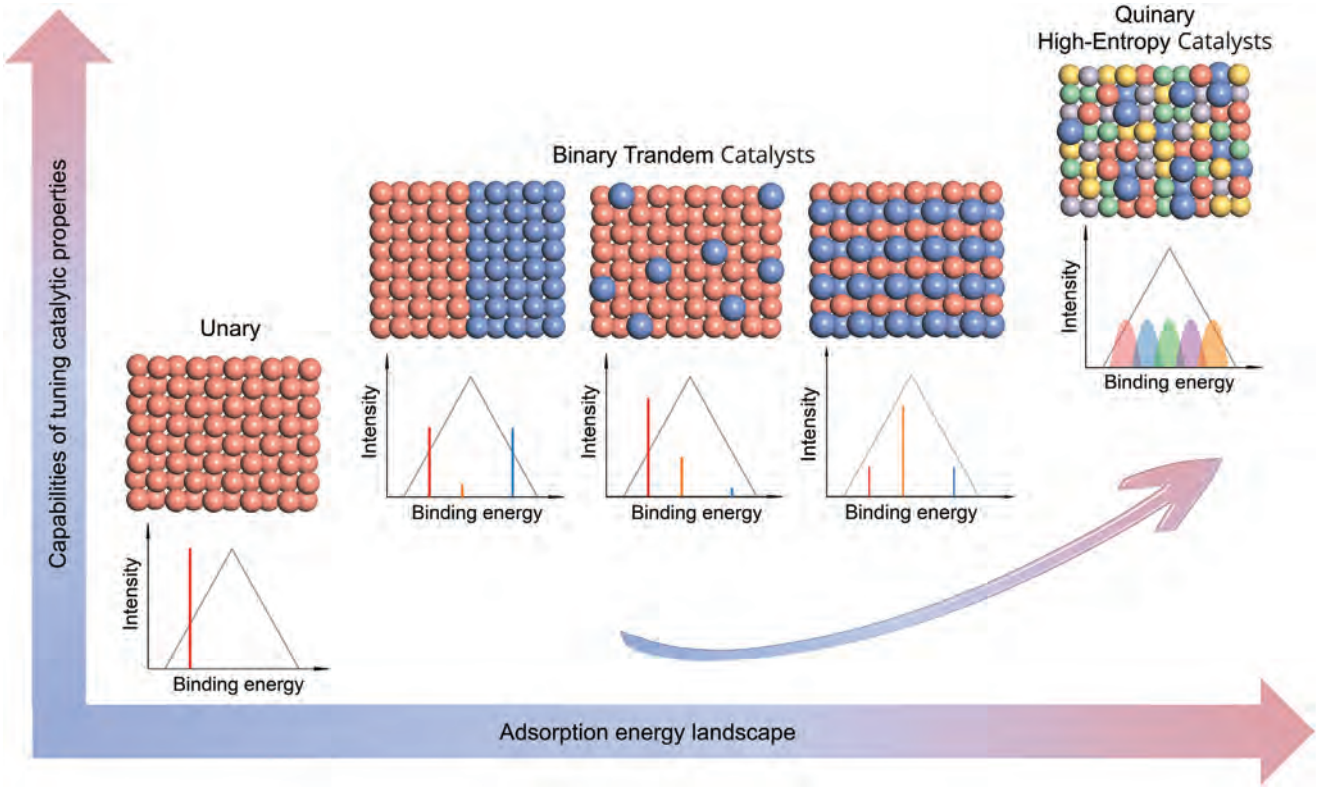

Figure 1. Relationship between the binding energy landscape and the electrocatalytic performance. The NO_3RR electrocatalytic activity of various kinds of catalysts increases with broadened adsorption landscape.

suffer from unclear reconstruction under operating conditions, limiting the rational design and catalytic activity of selective catalysts.[9,10] Moreover, binary active centers struggle to surpass the volcano-shaped performance curve in NO_3RR.[11]

A recent approach to overcoming scaling relations involves exploring the vast multi-dimensional composition space to develop high-entropy alloy (HEA) catalysts.[12–14] The entropic stabilization induced by alloying multiple elements creates a high kinetic diffusion barrier, promoting kinetic stabilization. Despite their catalytic potential, understanding the fundamental activity of HEA catalysts remains in its infancy, hindered by the elusive structure-activity correlation.[15,16] Many studies focus on isolated metal atoms, neglecting the strong d-d synergistic effects among multi-elemental compositions, which limits guidelines for designing effective active centers.[13,17] More importantly, the lack of strict limitations on interactions between active sites and reaction intermediates complicates the in-depth investigation of this correlation.[18] Particularly for the multi-step NO_3RR process, understanding how synergistic active sites in HEA tune the adsorption of specific intermediate species is complex. Therefore, the role of multi-functional active sites in HEA for efficient NO_3RR requires further exploration.

Here, we report the development of MnFeCoNiCu HEA for efficient and durable NO_3^- reduction. This multi-metallic alloy leverages unique multi-elemental interactions to subtly adjust the adsorption energy, deviating from general energy-scaling relations. As shown in the volcano plot with bridge-bidentate $^*NO_3$ adsorption energies and limiting potential as descriptors, multiple pair-metal sites in the HEA are positioned near the peak of the limiting potential volcano, indicating lower reaction barriers. The variation in local electronic structure broadens the adsorption energy landscape, creating multi-functional binding sites. Specifically, these multi-functional active centers, with reverse adsorption capabilities, act as cooperative sites for efficient NH_3 electrosynthesis. The MnFeCoNiCu HEA catalyst delivers an impressive NH_3 Faradaic efficiency of 94.5 ± 4.3% and a yield rate of 10.2 ± 0.5 mg h^{-1} mg_{cat}^{-1}. It also demonstrates remarkable stability over 250 h in an integrated reactor, achieving simultaneous NO_3^- reduction and NH_3 recovery.

2. Results

2.1. Computational Insights into the NO_3RR Activity Origin on Multi-Functional Active Sites of HEA

To elucidate the correlation between the multi-elemental mixing-induced synergistic effect in HEAs and electrocatalysis performance, we performed Density functional theory (DFT) calculations (Methods). The earth-abundant transition metal (Mn, Fe, Co, Ni, Cu)-based catalysts have been widely visioned as the leading choices for NO_3^- reduction.[19–23] In that way, we chose those five elements for designing HEA compositions. Table S1 (Supporting Information) exhibits the disordered atomic arrangement and the optimized structural configuration of HEA and pure metal used for the DFT calculations. We first calculated the

charge density distributions of surface atoms in pure metals and HEA to investigate the local electronic environment modulation of multiple elements at an atomic level (Figures 2a and S1, Supporting Information). Compared with mono-metal, a charge redistribution on HEA was observed. In detail, both Mn and Fe atoms in HEA possess a lower electron density than pure metals. In contrast, Co, Ni, and Cu atoms in HEA enable a higher concentration of local electron density. It should derive the electrons transfer from Mn and Fe to Co, Ni, and Cu atoms.[24–26] Bader charge analysis further estimates the changed charge of every surface atom in the MnFeCoNiCu HEA (Figure 2b). Each metal element exhibits the same tendency of the electronic structure change, while the transferred charge quantities for each element are distributed in a wide range depending on the different elemental coordination environments.[27] For example, the Ni atoms gain charge in the range of 0.09 to 0.17 |e|, and the charge loss of Mn atoms ranges from 0.18 to 0.29 |e|. Accordingly, the electronic perturbation from the various metal species demonstrates the local electronic structure modulation at an atomic level.

The significant redistribution of electrons in the multi-elemental mixing system was further evidenced by the partial projected density of states (PDOSs) results (Figure 2c). The Mn and Fe sites dominate at adjacent positions near the Fermi level (E_F). In contrast, Co, Ni, and Cu sites take up deeper positions far away from E_F. The 3d-orbitals of those elements could be coupled into a near-continuum distribution in the broad coverage through d-d orbital hybridization.[28] Notably, a large orbital overlapping among different metals improves the atom-to-atom electron transfer in the MnFeCoNiCu HEA. A detailed study of the site-dependent PDOSs of each element and the related d-band center model was used to describe the electronic interaction between the adsorbate and metal (Figure 2d).[29] The d-band center (ε_d) positions of pure Mn, Fe, Co, Ni, and Cu relative to EF were calculated to be −0.87, −0.98, −1.02, −1.13, and −2.33 eV, respectively, which clearly illustrates that Mn and Fe have stronger adsorption ability than Co, Ni and Cu. Compared to the d-band center positions of pure metals, the d-states of Mn ($\varepsilon_d = -0.66$ eV) and Fe ($\varepsilon_d = -0.83$ eV) with high adsorption energies in the HEA are much closer to E_F, leading to the strengthened adsorption of NO_3RR intermediates. While Co ($\varepsilon_d = -1.05$ eV), Ni ($\varepsilon_d = -1.35$ eV), and Cu (εd = −2.45 eV) with low-lying d-band positions display evident downshifts in the d-band centers.[30] The opposite trend entails weakening adsorption strength in these three sites. The variations of local electronic structures indicate the broadband adsorption energy landscape in the multi-elemental mixing HEA, which is particularly promising for catalysis in multi-step NO_3RR, requiring various binding energy levels.[31]

NO_3RR is a complex 8-electron transfer reaction that can result in a wide range of byproducts and several possible pathways.[32] In that way, this system's most possible reaction pathway was first implied. The tested HEA samples were exhibited in the following section and the Methods part. The differential electrochemical mass spectrometry (DEMS) detected the various mass-to-charge (m/z) signals of 17, 30, 33, 44, and 46 correspond to NH_3, NO, NH_2OH, N_2O, and NO_2, respectively (Figure S2, Supporting Information).[33] Notably, the NH_3 signal was the strongest, confirming the higher NH_3 selectivity. In addition, NO_2, NO, and NH_2OH are important intermediates for the NO3RR, while the intensity of those signals is lower than that of NH_3. Those intermediates quickly convert to the final product, NH_3, without accumulation. Besides, the signal belonging to N_2O (m/z = 44) is insignificant, which is an important intermediate for NO_3^--to-N_2. This means that the selectivity of N_2 products is low. In-situ Raman spectroscopy probed the symmetric bending vibrations of HNH at ≈1363 cm^{-1} and the N = O stretch of HNO at ≈1585 cm^{-1}, as depicted in the following section (Figure S3, Supporting Information).[34] Based on those analyses, the proposed NO_3RR process in this system is depicted as the following path: NO_3^-→ $^*NO_3$→ $^*NO_2$→ $^*NO$ → $^*NOH$→ $^*NH_2O$→ $^*NH_2OH$→ $^*NH_2$→ $^*NH_3$→ NH_3 (**Figures 2e** and S4 and S5, Supporting Information). The limiting potential for NO_3RR toward NH_3 is 0.65 eV. The pathways to other possible byproducts, NO_2, NO, and N_2, are also drawn for comparison. In contrast, the higher energy barriers for the formation of NO_2 (1.88 eV), NO (2.42 eV), and N_2 (2.58 eV) on the same absorption sites, inhibit the formation of those by-products, consistent with the products analysis in electrolysis tests.

Theoretical calculations are further applied to illustrate the reactivity properties of multiple active sites in HEA for NO_3RR.[8] In this multi-step conversion, NO_3^- is first adsorbed and discharged to generate $^*NO_3$, an essential prerequisite for further charge transfer.[19,35] The bridge-bidentate binding sites present noticeable electron depletion with the NO_3^- adsorption, which attests that these direct binding atoms are the main sites contributing to the charge transfer during adsorbing.[36] Thus, the adsorption of bridge-bidentate $^*NO_3$ on 15 unique coordination environments of HEA was studied (Figure S6 and Table S2, Supporting Information). Notably, a broadened adsorption-free energy landscape for $^*NO_3$ (ΔE_{*NO3}) at various sites in HEA surfaces is shown as a heat map in Figure S7 (Supporting Information). Due to the adsorption energy scaling relations in multi-step NO_3RR, the adsorption of NO_3^- cannot be used to represent the catalytic activity of the whole conversion process. The Bayesian theory of chemisorption identified the linear scaling relations of adsorption energies between $^*NO_3$ and $^*N$ for various metals,[37] and those two species can be regarded as reactivity descriptors to unravel the adsorption-energy scaling relations in NO_3RR.[29] For monometallic catalysts, there is a significant linear scaling of adsorption energies between $^*NO_3$ and $^*N$, with a slope of 1.58 (R^2: 0.97), which is quite close to the theoretical slope of 1.53 (Figure 2f). Various binding active sites in HEA are predicted to present reactivity properties beyond the scaling relations, especially those heteronuclear active sites, such as Mn-Fe, Co-Ni, and Fe-Cu pairs. As suggested by the interatomic interaction prediction, the increased d-center of site Mn and Fe atoms in HEA enhances the stabilization of $^*NO_3$ while the coupled atoms Co, Ni, and Cu with evident downshifts in the d-band centers interact in a primarily repulsive manner, leading to an independent tuning of the $^*NO_3$ and $^*N$ binding energies.

To further verify the adsorption energy-activity relationship for HEA with broadband adsorption energy, selecting $^*NO_3$ as a descriptor, a volcano plot of limiting potential for NO_3RR is constructed (Figures 2g and S8–S27, Supporting Information). In the monometallic catalysts system, theoretical analysis found that one specific site possesses stronger adsorption ability, thus decelerating nitrogen-bonded species release and increasing the

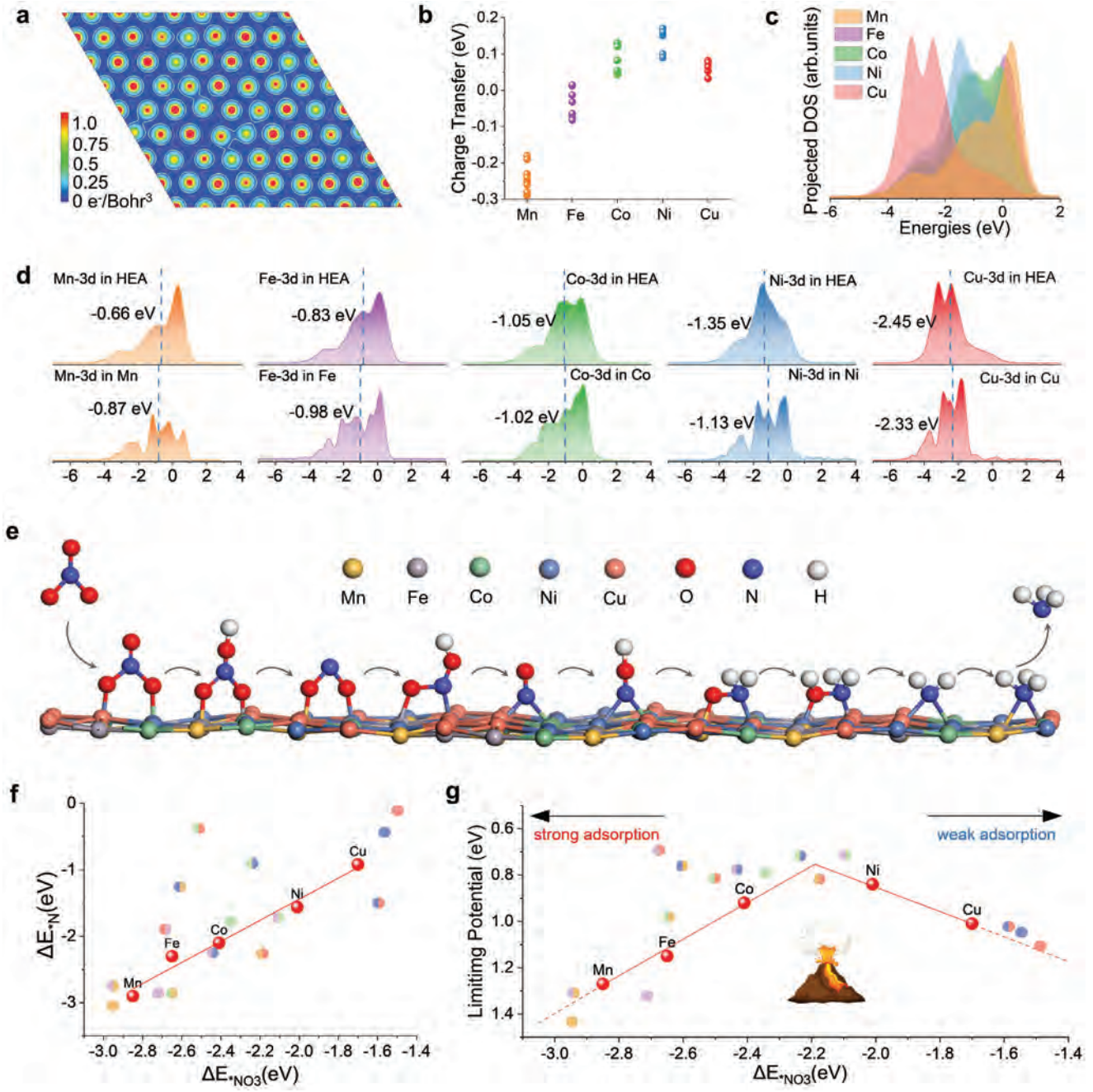

Figure 2. DFT calculations of the MnFeCoNiCu HEA model. a) Electron density of the MnFeCoNiCu HEA. b) Bader charge analysis of the MnFeCoNiCu HEA. c,d) A comparison of computed PDOS of each element in the HEA and pure metals (Mn, Fe, Co, Ni, and Cu). e) The overall roadmap for NO_3^--to-NH_3 conversion over the HEA catalyst. f) DFT-calculated adsorption energies of $^*NO_3$ and $^*N$ on pure metal (red ball) and various binding active sites in the HEA (Mn: yellow; Fe: Purple; Co: green; Ni: blue; Cu: red). g) The activity volcano plot of NO_3RR on the pure metal and HEA using the bridge-bidentate NO_3^- as a descriptor.

energy barriers of the following hydrogenation/dehydration steps, whereas too weak adsorption results in the large energy barrier of NO_3^- adsorption and slowing down the reaction. The reaction is impeded in both instances. This is consistent with the above-mentioned adsorption energy scaling relation in the multi-step NO_3RR. Multiple pair-metal sites in HEA are predicted to be close to the top of the activity volcano plot with proper binding energy levels to balance the adsorption and desorption process.[38] In addition, the multi-functional active centers in the MnFeCoNiCu HEA work as cooperative sites that enable efficient NH_3 electrosynthesis. For example, the Mn-Mn ($\Delta E_{*NO3} = -2.95$ eV) and Fe-Fe ($\Delta E_{*NO3} = -2.72$ eV) sites with stronger adsorption ability are suitable for adsorbing intermediates, whereas the nearby Cu-Cu ($\Delta E_{*NO3} = -1.49$ eV), Ni-Ni

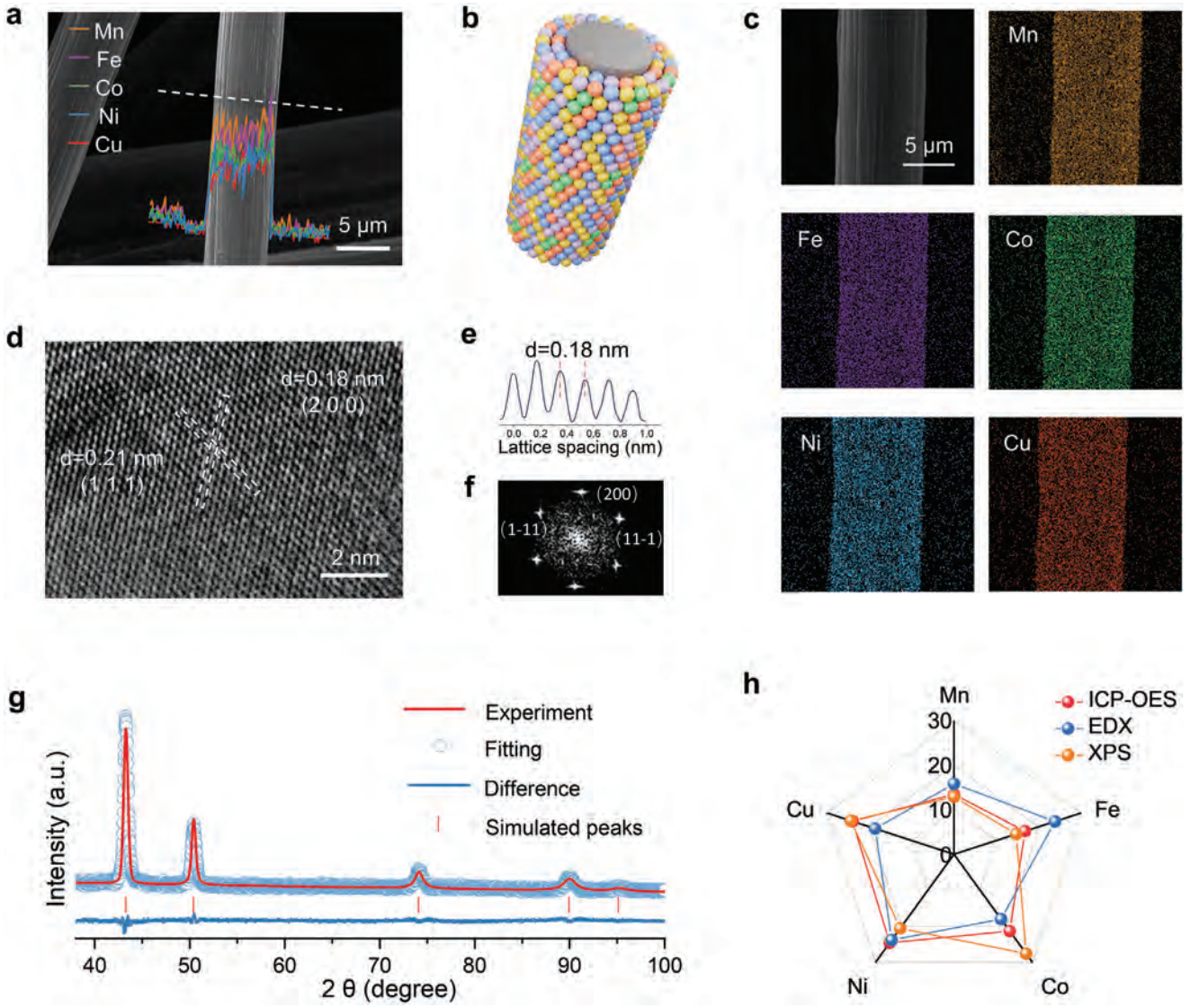

Figure 3. Characterization of the HEA. a) FE-SEM image of the MnFeCoNiCu HEA. The inset shows the SEM-EDS line-scanning analysis of the MnFeCoNiCu HEA, and the white line represents the line-scanning direction. b) The schematic diagram of the synthesized MnFeCoNiCu HEA. c) FE-SEM image and corresponding EDS elemental mappings of the MnFeCoNiCu HEA. d) STEM image of the HEA. e STEM image of the MnFeCoNiCu HEA. e) The intensity profiles of the MnFeCoNiCu HEA are shown in d. f) The SAED pattern of the MnFeCoNiCu HEA. g) XRD pattern of the MnFeCoNiCu HEA with detailed Rietveld refinements. h) Atomic percentages of various metals in the MnFeCoNiCu HEA as determined by ICP-OES, EDS, and XPS.

(ΔE_{*NO3} = −1.81 eV) and Cu-Ni (ΔE_{*NO3} = −2.05 eV) metal pairs with lower binding energy act to refresh the surface of catalyst, in turn breaking the traditional scaling relationships.[20] In all, this multi-metal system with a broadened adsorption energy landscape enables a desirable trade-off between the adsorption and desorption of multiple intermediates, thus avoiding the adsorption-energy scaling limitations for effective NH_3 electrosynthesis.

2.2. Synthesis and Characterization of the MnFeCoNiCu HEA

As a proof of concept, we synthesized the MnFeCoNiCu HEA on carbon papers (Methods). A simple and fast direct current magnetron sputtering method was applied to deposit the MnFeCoNiCu HEA. The scanning electron microscopy (SEM) image of the as-deposited sample in **Figures** 3a and S28 (Supporting Information) verified HEA uniformly anchored across the entire carbon networks. The thickness of the HEA catalyst was evaluated by SEM and was ≈50 nm (Figure S29a, Supporting Information). The schematic diagram of synthesized HEA is illustrated in Figure 3b. The line-scanning and SEM-energy-dispersive spectroscopy (SEM-EDS) show the homogeneous distribution of Mn, Fe, Co, Ni, and Cu elements, indicating that all five elements are well-mixed without composition segregation in HEA (Insert in Figure 3a,c).[39] We then conducted transmission electron microscopy (TEM) to elucidate the crystal structure and multi-elemental distribution of HEA. The TEM image shows distinctly

visible lattice fringes with an interplanar crystal spacing of 2.1 and 1.8 Å, corresponding to the (111) and (200) plane of the fcc phase (Figure 3d,e). The selected area electron diffraction (SAED) pattern also identified the fcc crystal structure of HEA (Figure 3f). The X-ray diffractometer (XRD) spectra of the as-deposited HEA sample exhibit the peaks relating to a face-centered cubic (fcc) HEA structure (Figure 3g).[40] The related XRD detailed Rietveld refinements also confirm the single fcc phase of HEA without phase-segregated structures.[41] The refined direct cell lattice constant for HEA is found to be a = b = c = 3.612 Å (Table S3, Supporting Information). In addition, the fcc diffraction peaks of the HEA shift slightly to lower angles due to the lattice distortions originating from the incorporation of multiple atoms. The elemental compositions of HEA were further measured by inductively coupled plasma-atomic emission spectroscopy (ICP-AES), energy dispersive X-ray spectroscopy (EDX), and X-ray photoelectron spectroscopy (XPS) (Figure 3h). These three methods exhibit the content of five principal elements in HEA have an atomic percentage in the range of 5% to 35% with the calculated mixing entropy (1.59R) larger than 1.5R, further demonstrating the intrinsic nature of HEA (Table S4, Supporting Information).

The chemical states and atomic structure of the MnFeCoNiCu HEA were further investigated by X-ray absorption spectroscopy (XAS) and XPS. The Mn, Co, Ni, Fe, and Cu K-edge X-ray absorption near-edge structure (XANES) of the MnFeCoNiCu HEA presents metallic pre-absorption edge features by comparing them with metal reference foils. Moreover, the Mn and Fe K-edge slightly shift to low energy, implying the local electron deficiency of Fe atoms in HEA (**Figures 4** and S30–S33, Supporting Information). Conversely, a minor shift of Cu, Co, and Ni K-edge toward high energy illustrates an increase in the local electron density in Cu, Co, and Ni atoms (Figures 4b and S30–S33, Supporting Information). Those shifts indicate the redistribution of the electron density in HEA.[17] The wavelet transforms (WT) of the extended X-ray absorption fine structure (EXAFS) spectra provided information on the *k*-space: only one Mn-M, Co-M, Ni-M, Cu-M, and Fe-M region was observed in HEA, suggesting the metallic state of Mn, Co, Ni, Fe and Cu atoms in HEA (Figures 4c,d and S30–S33, Supporting Information). In addition, confirming the lower Cu-M region (R≈2.1 Å) in HEA as compared to the Cu ($R \approx 2.3$ Å), the lower Ni-M region (R≈2.2 Å) in HEA as compared to the Ni ($R \approx 2.3$ Å), the higher Mn-M region (R≈2.4 Å) in HEA contrasts with Mn ($R \approx 2.2$ Å), and the higher Fe-M region (R≈2.4 Å) in HEA contrasts with Fe ($R \approx 2.2$ Å) were observed in the coordination shell, respectively. This trend indicates the nature of interatomic interaction in HEA.[28] The corresponding EXAFS of Mn, Co, Ni, Fe, and Cu were ascertained by fitting the Fourier transform (FT) spectra. As shown in Figures 4e,f and S31–S33 (Supporting Information), the FT-EXAFS spectra of Mn, Co, Ni, Fe, and Cu atoms in HEA only show the metallic bond, and the average bond length quite deviates from the metallic bond in bulk Mn, Co, Ni, Fe, and Cu samples, indicating that Mn, Co, Ni, Fe, and Cu elements are binding with different metal atoms. The XPS spectrum of the MnFeCoNiCu HEA confirms the presence of Mn, Fe, Co, Ni, and Cu elements (Figure 3g). To better investigate the electronic structure modulation of these principal elements in HEAs, we compare the binding energies of the FeCoNiCuMn HEA and pure metals for each element (Figures 3h and S34, Supporting Information). The core levels of Mn 2p and Fe 2p in HEA shift to a higher binding energy than metallic Mn and Fe, indicating the local electron deficiency of Mn and Fe. Conversely, Co 2p, Ni 2p, and Cu 2p exhibit a negative shift to lower binding energy and illustrate an increase in the local electron density.[42] Such a trend is in agreement with the XAS analyses. Moreover, only small amounts of high valency for metal elements were observed, which could be ascribed to partial surface oxidation during the XPS experiments.[43] The Raman spectrum of the fresh HEA exhibits no obvious characteristic peaks from 200 to 1000 cm^{-1}, confirming that no metal oxides exist in the HEA catalyst (Figure S35, Supporting Information).

2.3. Application of the MnFeCoNiCu HEA@C in NO_3RR

To investigate the NO_3RR activity of the MnFeCoNiCu HEA, a standard three-electrode H-type cell was employed for an electrochemical test under ambient temperature and pressure (Figures S36, Supporting Information and Methods). Unless noted, all potentials were referenced to the reversible hydrogen electrode (RHE). Linear sweep voltammetry (LSV) was first conducted to study the activity of as-synthesized HEA catalyst in the presence and absence of NO_3^- (Figure S37, Supporting Information). The obtained curves show that the HEA has the highest increase of current density in a wide range from −0.1 and −0.8 V. Notably, a sharply increased current density for the hydrogen evolution reaction (HER) at around −0.7 V in NO_3^- free solution. The HEA requires a much lower potential to drive the NO_3RR than the competing HER, indicating that HER can be inhibited at a relatively low overpotential for the high selectivity of NO_3RR.[34,44] Additionally, NO_3RR performance was assessed using LSV with HEA and pure metal electrocatalysts (Figure S38, Supporting Information). The current density of the HEA electrode was much higher than other electrocatalysts over a broad range of negative potentials, demonstrating the high catalytic activity of HEA toward NO_3RR. One hour of electrolysis was further performed to evaluate the activity and selectivity of the as-synthesized catalysts. According to the LSV curves, the NH_3 Faradaic efficiency (FE) of HEA and other pure metals catalysts were investigated across a wide potential range from 0 to −0.80 V (**Figure 5a**). When potential negative shifts, the FE for NH_3 shows a volcanic shape curve with a maximum value at −0.6 V. Further decreasing the potential to −0.8 V, a sharp decline of the NH_3 FE indicates that the nitrate reduction to ammonia is challenged by the drastic enhanced HER at a higher applied potential. The HEA offers an FE of NH_3 of 94.5 ± 4.3% at −0.6 V, obviously over other pure metals catalysts. The superiorities of HEA catalyst in NO_3RR prove that the multi-elemental mixing-induced synergistic effect for HEA could effectively promote the electrochemical NO_3^- reduction. At −0.6 V, the HEA reach NH_3 FE of 76.4 ± 2.8%, 78.2 ± 2.4%, 87.6 ± 2.1%, 91.5 ± 3.4%, and 94.5 ± 4.3% in 5, 10, 25, 50, and 100 mM NO_3^-. The NH_3 yield rate linearly increases when the NO_3^- concentration increases from 5 to 100 mM with a maximum ammonia-evolving rate (Y_{NH3}) of 10.2 ± 0.5 mg h^{-1} mg_{cat}^{-1} (Figure S39, Supporting Information). The high NH_3 FE and Y_{NH3} of HEA at different NO_3^- concentrations indicate the wide application range for NO_3^- removal. The electrochemical impedance spectroscopy (EIS) was performed

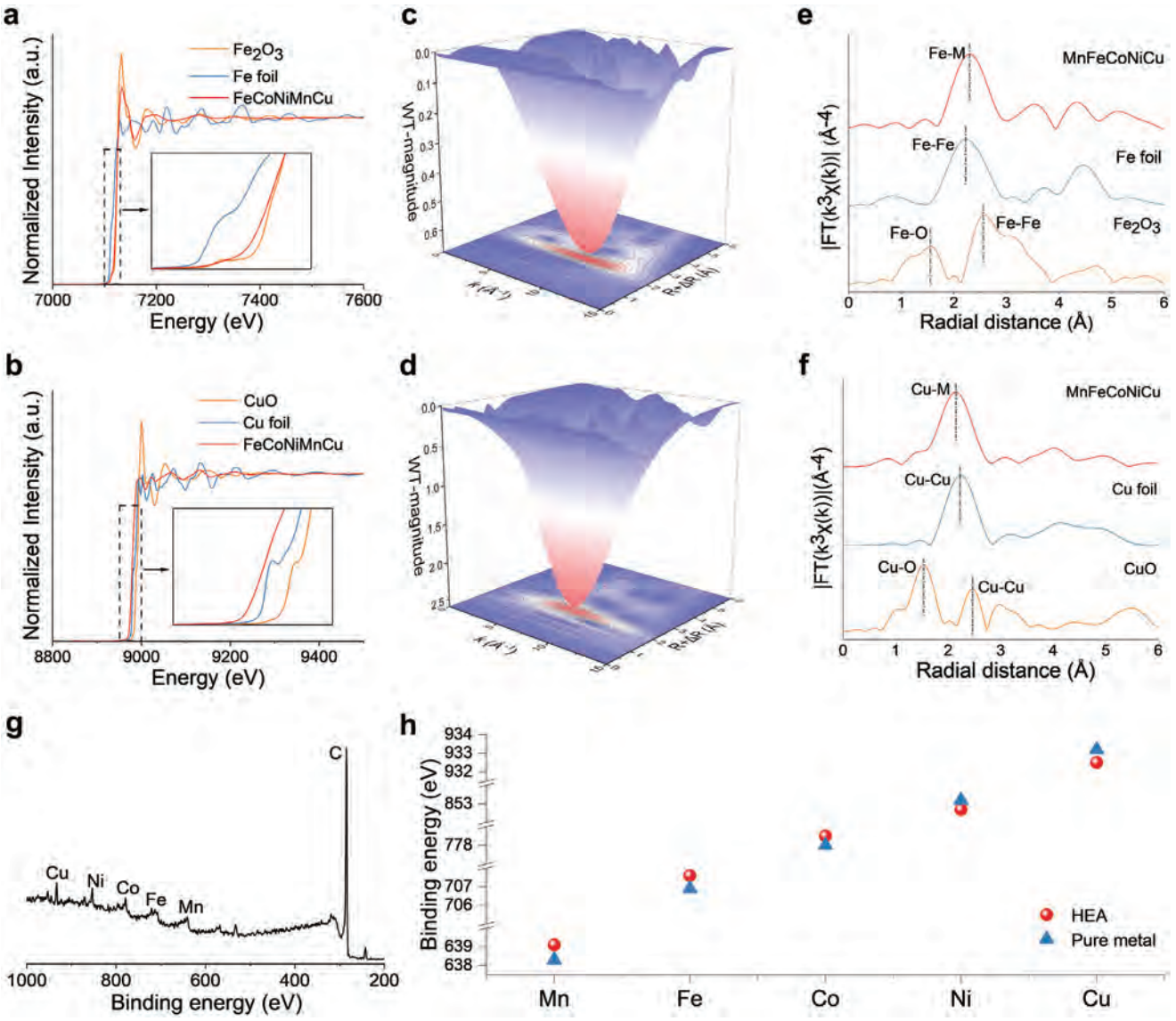

Figure 4. Characterization of chemical states of the HEA. a) Cu K-edge XANES spectra of the Cu foil, CuO, HEA. b) Fe K-edge XANES spectra of the Fe foil, Fe_2O_3, HEA. c) Wavelet transforms of the k^3-weighted EXAFS signals of Cu in the HEA. d) Wavelet transforms of the k^3-weighted EXAFS signals of Fe in the HEA. e) FT-EXAFS spectra of the Cu foil, CuO, and HEA in the 0–6 Å region. f) FT-EXAFS spectra of the Fe foil, Fe_2O_3, HEA in the 0–6 Å region. g) A survey of high-resolution XPS spectra of the MnFeCoNiCu HEA. h) A comparison of the binding energy of each element in the MnFeCoNiCu HEA and pure metals.

to support the remarkable electrocatalytic activity of HEA. As shown in Figure S40 (Supporting Information), the Nyquist plots of the prepared electrodes exhibit a smaller charge-transfer resistance (Rct) on HEA (1.98 Ω) compared to Mn (7.24 Ω), Fe (6.62 Ω), Co (5.78 Ω), Ni (6.15 Ω), and Cu (2.53 Ω). The HEA catalyst has fast electron transport in the catalytic process and thus accelerates the sluggish reaction kinetics. Moreover, the performance of FeCu, CuFeCo, CuFeCoNi, and CuFeCoMn as electrocatalysts for NO_3RR were studied. Those controlled samples were fabricated using the magnetron sputtering technique with the corresponding alloy targets. Other deposition conditions are the same as those of MnFeCoNiCu HEA. One hour of electrolysis was performed to evaluate the activity and selectivity of those multi-metal catalysts. The amperometric curve (i-t) measurements were conducted in the 0.5 M Na_2SO_4 electrolyte containing 0.1 M NO_3^- concentrations under the same applied potential of −0.6 V. The NH_3 Faradaic efficiency and ammonia-evolving rate of MnFeCoNiCu HEA is much higher than those binary, ternary, and quaternary Cu alloys (Figure S41, Supporting Information). To further characterize the intrinsic activities of these catalysts, the specific activities were normalized by the electrochemical active surface area (ECSA) (Figure S42, Supporting Information).[45] As expected, the HEA exhibits the most favorable NO_3^--to-NH_3 conversion, with the highest normalized partial current density of NH_3 in the entire potential region (Figure 5b). As a proof of concept, we used

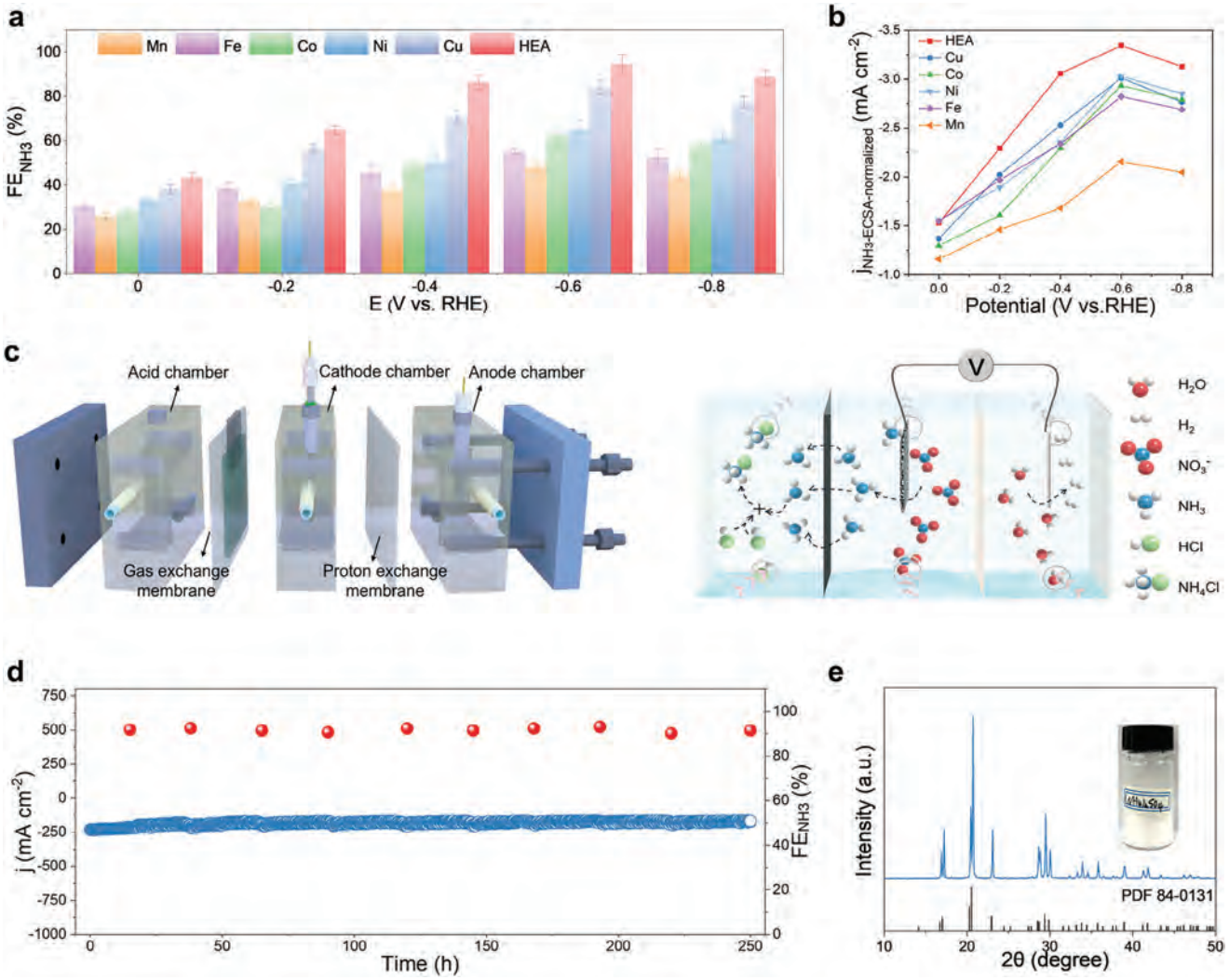

Figure 5. Electrocatalytic NO_3^--to-NH_3 conversion. a) NH_3 Faradaic efficiency of the Mn, Fe, Co, Ni, Cu, and MnFeCoNiCu HEA in 0.5 M Na_2SO_4 electrolyte with 0.1 M NO_3^- upon a scan rate of 5 mV s^{-1}. b) Partial current densities of NH_3 at various applied potentials over the Mn, Fe, Co, Ni, Cu, and MnFeCoNiCu HEA. c) Schematic of the integrated three-chamber reactor by coupling electrocatalysis with ammonia recovery unit. d) Long-term stability test (250 h) of the MnFeCoNiCu HEA electrode under the applied potential of −0.6 V versus RHE using the integrated device. e) XRD pattern of the obtained $(NH_4)_2SO_4$ powder.

configurational entropy as descriptors to study the MnFeCoNiCu materials in various element ratios. $Mn_{0.05}Fe_{0.05}Co_{0.3}Ni_{0.3}Cu_{0.3}$ (R = 1.36), $Mn_{0.11}Fe_{0.13}Co_{0.25}Ni_{0.28}Cu_{0.23}$ (R = 1.55), $Mn_{0.21}Fe_{0.23}Co_{0.19}Ni_{0.19}Cu_{0.18}$ (R = 1.61), $Mn_{0.26}Fe_{0.26}Co_{0.16}Ni_{0.16}Cu_{0.16}$ (R = 1.58) and $Mn_{0.34}Fe_{0.35}Co_{0.1}Ni_{0.11}Cu_{0.09}$ (R = 1.42) were synthesized (Figures S43 and S44, Supporting Information). Upon possessing the MnFeCoNiCu materials with adjustable configurational entropy, their electrocatalytic performance for NO_3^--to-NH_3 conversion was evaluated. It can be seen that $Mn_{0.21}Fe_{0.23}Co_{0.19}Ni_{0.19}Cu_{0.18}$ offer a FE of NH_3 of 94.5 ± 4.3% higher than $Mn_{0.05}Fe_{0.05}Co_{0.3}Ni_{0.3}Cu_{0.3}$ (84.4 ± 4.2%), $Mn_{0.11}Fe_{0.13}Co_{0.25}Ni_{0.28}Cu_{0.23}$ (90.2 ± 3.4%), $Mn_{0.26}Fe_{0.26}Co_{0.16}Ni_{0.16}Cu_{0.16}$ (90.4 ± 2.4%) and $Mn_{0.34}Fe_{0.35}Co_{0.1}Ni_{0.11}Cu_{0.09}$ (86.4 ± 2.8%) electrodes (Figure S45, Supporting Information). Meanwhile, the NH_3 yield rate on $Mn_{0.25}Fe_{0.25}Co_{0.25}Ni_{0.25}Cu_{0.25}$ is 10.2 ± 0.5 mg h^{-1} mg_{cat}^{-1}, notably surpassing $Mn_{0.05}Fe_{0.05}Co_{0.3}Ni_{0.3}Cu_{0.3}$ (6.6 ± 0.5%), $Mn_{0.11}Fe_{0.13}Co_{0.25}Ni_{0.28}Cu_{0.23}$ (7.6 ± 0.4%), $Mn_{0.26}Fe_{0.26}Co_{0.16}Ni_{0.16}Cu_{0.16}$ (6.9 ± 0.2%) and $Mn_{0.34}Fe_{0.35}Co_{0.1}Ni_{0.11}Cu_{0.09}$ (6.28 ± 0.3%). These results demonstrate that HEA with large entropy enables good NO_3^-RR efficiency and selectivity as DFT-predicted. To study the relationships between the NO_3^-RR activity and stability, accelerated durability tests (ADTs) were applied to study the durability of MnFeCoNiCu alloys in various entropy regions (Figure S46, Supporting Information). Among them, $Mn_{0.21}Fe_{0.23}Co_{0.19}Ni_{0.19}Cu_{0.18}$ with the largest configurational entropy exhibits the best durability. After 2000 cycles, the NO_3^-RR activity loss of $Mn_{0.21}Fe_{0.23}Co_{0.19}Ni_{0.19}Cu_{0.18}$ is negligible, the normalized partial current density at −0.4 V is 64.3 mA cm^{-2}, which is smaller 3.1 mA cm^{-2} compared to the initial value. Meanwhile, MnFeCoNiCu alloys with other atomic ratios exhibit

a larger loss of active current density. In that way, the $Mn_{0.25}Fe_{0.25}Co_{0.25}Ni_{0.25}Cu_{0.25}$ with the largest entropy breaks the activity-stability scaling relations and simultaneously enhances NO_3^-RR performance and electrocatalytic durability.

To trace the source of the NH_3, an isotope labeling experiment was conducted with $^{14}NO_3^-/^{15}NO_3^-$ in a ratio of 1 to 1 as the N source and $C_4H_4O_4$ as the internal standard. ^1H nuclear magnetic resonance (NMR) spectroscopy of the prepared solution after electrolysis shows doublet peaks with a coupling constant of 73 Hz and triple patterns with a coupling constant of 52 Hz, which correspond to the signal of $^{15}NH_4^+$ and $^{14}NH_4^+$, respectively. The unchanged ratio of $^{14}NH_4^+/^{15}NH_4^+$ products confirms that added NO_3^- is the only source of nitrogen for ammonia electrosynthesis here (Figure S47, Supporting Information). Colorimetric methods and ^1H NMR quantification of NH_3 were compared (Figures S48 and S49, Supporting Information). The concentration of generated NH_3 determined by those two quantitative methods is very close, evidently proving the accuracy of NH_3 detection (Figure S50, Supporting Information). Little to no signal of NH_3 after electrolysis in blank Na_2SO_4 solution once again identifies the obtained NH_3 originated from NO_3RR instead of any other ammonia pollution.

To confirm the multi-functional active centers in the MnFeCoNiCu HEA, the Raman scattering peaks were observed in NO_3RR on the MnFe, CoNiCu, and MnFeCoNiCu HEA. The signals of NO_3^- and SO_4^{2-} in the solution and other intermediates adsorbed on the catalysts' surface were observed in the spectra between 900 and 1800 cm^{-1}. With the decreasing of potential from open circuit potential (OCP) to −0.7 V, several peaks came out in sequences in HEA catalysts (Figure S3, Supporting Information). First, the obvious peak observed at ≈990 and 1052 cm^{-1} was attributed to the SO_4^{2-} and NO_3^- species in solution at OCP. After that, when the potential was decreased, the NO_3^- species in the solution began to adsorb on the surface of the HEA catalyst with the symmetric NO_3^- stretching of $^*NO_3^-$ closed to 1005 cm^{-1}. Meanwhile, the symmetric bending vibrations of HNH at around 1363 cm^{-1} and the N = O stretch of HNO at ≈1585 cm^{-1} appeared as the working potential shifted negatively, meaning the formation of HNO intermediate and NH_3 product. The Raman spectra on the MnFe catalyst (Figure S51a, Supporting Information) were similar to the spectra of the HEA catalyst. Still, the peak related to HNO and NH_3 appeared at a higher overpotential (−0.5 V) due to its poor ability for deep $^*NO_3^-$ hydrodeoxidation properties. Conversely, the HNO and NH_3 peaks in CoNiCu catalysts were generated at −0.1 V (Figure S51b, Supporting Information). The intensity of $^*NO_3^-$ at lower potentials was very weak, indicating that a low amount of $^*NO_3^-$ species was absorbed on the surface of CoNiCu. Those results are consistent with the DFT calculation results. Thus, the cooperation of multi-functional active sites in MnFeCoNiCu HEA enables optimal adsorption-desorption behavior of multiple intermediates for efficient NO_3^--to-NH_3 conversion.

To unveil the possible relationship between thickness and stability, inductively coupled plasma-optical emission spectroscopy (ICP-OES) was employed to track metal content in the electrolyte during reproducible electrolysis (Figure S52, Supporting Information). The results suggest that three samples with 50, 100, 150, and 200 nm HEA films exhibit similar metal elements dissolution after 24 h NO_3^-RR. Thus, the thickness of HEA films in the range of 50–200 nm has no significant effect on the stability of the catalytic reaction. Moreover, to better estimate the real lifetime of MnFeCoNiCu HEA catalysts, we further conduct the electrochemical reaction in a typical H-type cell and refresh the electrolyte after 24 h of electrolysis (Figure S53, Supporting Information). Those two chambers include a 40 mm^3 anode chamber and a 40 mm^3 cathode chamber. The anode cell contained 0.5 M Na_2SO_4, and the cathode contained 0.5 M Na_2SO_4 with 0.5 M NO_3^-. The current density of HEA attenuated during 24 h of electrolysis due to the rapid depletion of NO_3^- in the electrolyte, but it returned to its initial value, refreshing the electrolyte. The chronoamperometric curves of HEA-NPs during the NO_3RR have almost no change, and the high durability of NH_3 FE was evidenced by a decrease of less than 10% after 12 cycles (each cycle lasting 24 h). Thus, the lifetime of these HEA catalysts was verified to last ≈288 h in this electrolysis condition. Furthermore, in-situ Raman spectroscopy was also applied to determine potential changes in the HEA catalysts. Except for the peaks corresponding to adsorbed SO_4^{2-}, NO_3^- and adsorbed $^*NO_3^-$, no other signals indicative of newly formed phases in HEA are observed in the spectra, affirming the robust structural stability of this multielement alloy (Figure S54, Supporting Information).

Besides the electrode performance, separation and recovery of the NH_3 product are also essential for the practical application of NO_3RR. From this aspect, we designed an integrated three-chamber device by coupling electrocatalysis with an ammonia recovery unit to continuously collect ammonia products, as schematically illustrated in Figures 5c and S55 (Supporting Information). The stability of HEA was assessed with this coupled reactor under industrial-relevant current densities.[46,47] This catalyst could robustly work at a high current density at≈250 mA cm^{-2} for up to 250 h with a high FE_{NH3} of 90%, confirming its applicability at the industrial level (Figure 5d). The SEM images of HEA after the long-term stability test show that the morphology is still unchanged, and the corresponding EDS mapping shows that the elemental content remains, demonstrating the excellent stability of this catalyst (Figure S56, Supporting Information). Moreover, increasing NO_3^- concentration from 0.5 to 1 M to test the stability of HEA catalysts in an integrated three-chamber reactor assembled with the flow-through NO_3^- reduction electrolyze and a membrane-based ammonia absorption unit to continuously produce and capture ammonia products. Due to the increased NO_3^- concentration, the related current density further increases to the industrial-relevant level (≈500 mA cm^{-2}). In this harsh operation condition, HEA catalyst still achieved over 200 h of long-term stability with over 90% FE_{NH3} maintained, confirming its applicability at the industrial level (Figure S57, Supporting Information). Such excellent long-term stable activity outperforms other reported electrocatalytic NO_3^--to-NH_3 conversion (Tables S5–S7, Supporting Information). During this electrocatalysis process, in-situ generated NH_3 products spontaneously permeate to the acid absorption chamber and are trapped in an H_2SO_4 solution. After further rotary evaporation, the outflowing $(NH_4)_2SO_4$ liquid from the recovery chamber was converted into high-purity solid $(NH_4)_2SO_4$ products with a collection efficiency of over 90%, as confirmed by the XRD pattern (Figure 5e).[48] Overall, these findings demonstrated the feasibility of directly converting nitrate-containing wastewater to useful

ammonia fertilizers in the assembly device by utilizing the active HEA catalyst.

3. Discussion

In summary, we fabricated a highly active and durable catalyst of the MnFeCoNiCu HEA on a carbon electrode, which features unconventional multi-elemental mixing states for optimizing multi-step NO_3RR. Its multi-elemental composition is randomly distributed in a single-phase HEA structure, resulting in diversity in local electronic structures and a broadened adsorption energy landscape. These multi-functional active sites in HEA enable optimal adsorption-desorption behavior of multiple intermediates, thus breaking the traditional scaling relationships in multi-step NO_3RR for efficient NO_3^--to-NH_3 conversion. This work offers an in-depth understanding of various interactions between multi-functional active sites on HEA surfaces and NO_3RR intermediates, opening a new avenue to achieve a breakthrough in energy-related applications.

4. Experimental Section

Materials Preparation: The precursors of the MnFeCoNiCu HEA were fabricated by direct current magnetron sputtering. The metal films were deposited by sputtering the MnFeCoNiCu alloy target with the nominal composition of equi-atomic (99.9% purity). The thickness of the film was controlled by the sputtering time and the deposition rate. A calibration curve was plotted using a series of films with different deposition times to quantify the deposition rate. The thickness of those films was 50, 100, 150, and 200 nm at the deposition time of 1, 2, 3, and 4 min, respectively (Figure S29, Supporting Information). The cross-sectional sample is artificially pre-cut and prepared vertically with sharp scissors. The deposition rate was 50 nm min^{-1}, the substrate was rotated at 15 rpm min^{-1}, and the substrate temperature was 573.15 K. The pressure of the chamber was reduced to 10^{-5} mTorr before deposition and kept at 10 mTorr in the sputtering process. The TM (TM = Mn, Fe, Co, Ni, Cu) catalysts were also synthesized for comparison. The preparation for TM (TM = Mn, Fe, Co, Ni, Cu) catalysts followed the same steps as the MnFeCoNiCu HEA synthesis, with the only difference being that single metal targets were used as metal sources in magnetron sputtering. Those controlled samples were fabricated using the magnetron co-sputtering technique on a carbon substrate, and pure commercial MnFe and CoNiCu alloy targets were used for co-sputtering. Different powers were applied to the MnFe and CoNiCu targets to obtain different Mn/Fe/Co/Ni/Cu ratios in the thin film samples. Other deposition conditions are the same as those of MnFeCoNiCu HEA.

Materials Characterizations: Morphology and elemental distribution were observed using scanning electron microscopy (SEM, FEI Quanta 450) and high-resolution transmission electron microscopy (HRTEM, JEOL-2800). The lattice arrangement was collected on High-angle annular dark-field scanning transmission electron microscopy (HAADF-STEM, atomic-resolution JEM-ARM300F2) at an accelerated voltage of 300 kV. Powder X-ray diffraction (XRD) with a Bruker D8 Focus Diffraction System was used for the crystalline structure analysis. The chemical composition of catalysts and the dissolved metal ions in the electrolyte were analyzed by an inductively coupled plasma atomic emission spectrometer (ICP-AES, PE optima 6000). XAFS measurements at Fe and Cu K-edge were performed at the 1W1B station of the Beijing Synchrotron Radiation Facility, China. The raw data analysis was conducted using the IFEFFIT software package, which used the ATHENA and ARTEMIS programs integrated within the Demeter packages according to the standard data analysis procedures. To obtain a radial distribution function, the Fourier transformation of the k_3-weighted EXAFS ($k_3\chi(k)$) from k space to R space was conducted. X-ray photoelectron spectroscopy (XPS, PHI 5000 Versaprobe) with monochromatic Al Kα radiation was used for chemical state analysis. All XPS spectra were calibrated with a C 1s line at 284.8 eV. A Shimadzu UV-3600 spectrometer was used to measure the UV–vis absorbance spectra at room temperature. Isotope labeling experiments were recorded using a nuclear magnetic resonance measurement (Bruker 400-MHz system). The differential electrochemical mass spectrometry (DEMS, QAS 100) identifies products and intermediates of continuous NO_3^- reduction. In-situ Raman spectroscopy was tested on a WITec alpha300 R Raman System under an excitation of 532 nm laser light.

Electrochemical Measurements: All the electrochemical measurements were carried out in an H-type electrolytic cell separated by a Nafion 117 membrane. A CHI660D electrochemical workstation was used to record the electrochemical response. In a typical three-electrode system, a HEA electrode, a saturated Ag/AgCl electrode, and a platinum foil acted as the working electrode, reference, and counter electrode, respectively. The loading of the HEA catalyst is ≈0.1 mg cm^{-2}. For accurate measurement, the weight difference of the 10 cm^{-2} carbon paper before and after sputtering was compared. The process was repeated three times to obtain the average value. All potentials in this study (versus saturated Ag/AgCl) were converted to the RHE reference scale by $E_{RHE} = E_{Ag/AgCl} + 0.0591 \times pH + E^0_{Ag/AgCl}$ ($E^0_{Ag/AgCl} = 0.197$). The electrochemical linear voltammetry (LSV) was performed at a rate of 5 mV s^{-1}. For the actual electrocatalytic NO_3^- reduction, the amperometric curve (*i–t*) measurements were conducted in the 0.5 M Na_2SO_4 electrolyte containing different NO_3^- concentrations (5, 10, 25, 50, and 100 mM) in the catholyte. To obtain the optimized conditions, the electrocatalytic activity of NO_3RR at the MnFeCoNiCu HEA@C catalyst was also evaluated under different applied potentials (−0, −0.2, −0.4, −0.6, −0.8 and −1.0 V vs **RHE**) for 1 h at a stirring rate of 400 rpm. Three replicate electrocatalytic tests were performed on each sample to determine the error bars.

Direct Ammonia Product Recovery in an Integrated Three-Chamber Reactor: The coupled electrochemical NO_3RR and in-situ NH_3 recovery process were conducted in a three-chamber reactor.[49] Those three chambers include a 20 × 20 × 20 mm^3 anode chamber, a 20 × 20 × 20 mm^3 cathode chamber, and a 20 × 20 × 20 mm^3 acid absorption chamber. The effective areas of the working electrode (MnFeCoNiCu HEA/C) and counter electrode (Pt) were ≈4 cm^2 (2 × 2 cm^2), and Ag/AgCl was used as the working electrode and reference electrode. The cathodic and anodic chambers were separated by a Nafion@117 cation exchange membrane, allowing protons to be transported from the anode to the cathode to balance the OH^- produced at the cathode, thus keeping the pH of the cathodic electrolyte constant. The anode cell contained 0.5 M Na_2SO_4, and the cathode contained 0.5 M Na_2SO_4 with 0.5 M NO_3^-. Moreover, the cathode chamber and acid adsorption unit were separated by a piece of commercial gas exchange membrane. The electrolyte flow rate and dilute H_2SO_4 (0.5 M) solution were all set as 60 ml min^{-1}. To obtain the final $(NH_4)_2SO_4$ solid, a rotary evaporator was utilized to dry the solution in the acid absorption chamber, and the solid product was quantified by XRD. The efficiency of NH_4^+ recovery (R) was calculated using the following equations:

$$R_{NH_4^+-N}\,(\%) = \frac{\text{collected dried } [(NH_4^+)_2)SO_4 \text{ in acid trap}}{NH_4^+ \text{ traped in acid adsorption room}} \quad (1)$$

Product Analysis—Determination of NO_2^-: The quantification of NO_2^- was conducted using the Griess method. A certain amount of electrolyte was diluted to the detection range and 5 mL diluted electrolyte, followed by adding 100 µL color reagent. A specific color reagent of the Griess method was prepared by mixing 10 mL phosphoric acid, 50 mL deionized water solution, 4 g p-aminobenzene sulfonamide, and 0.2 g N-(1-Naphthyl) ethylenediamine dihydrochloride. After standing for 20 min at room temperature, the absorbance value at 540 nm was determined by UV–vis absorption spectra. To quantify the amount of NO_2^-, a calibration curve was plotted using a series of standard concentration sodium nitrite ($NaNO_2$) solutions.

Product Analysis—Determination of NH_3: Similar to the approach of determining the concentration of NO_3^- and NO_2^-, the produced NH_3 was confirmed by the indophenol blue method. First, a certain amount of

electrolyte was removed from the cathodic compartment and diluted to the detection range. Then 2 mL diluted electrolyte was taken out into a test tube, next 1 mL 2.0 M NaOH solution containing 10.0 wt.% salicylic acid ($C_7H_6O_3$) and 10.0 wt.% sodium citrates ($C_6H_5Na_3O_7{\cdot}2H_2O$) was added to the aforementioned test tube, followed by adding 1 mL 0.05 M NaClO solution and 0.2 mL 1.0 wt.% sodium nitroferricyanide ($Na_2[Fe(NO)(CN)_5]{\cdot}2H_2O$) solution. After sitting for 2 h in a dark place, the absorption spectrum was recorded at a wavelength of 658 nm using a UV–vis spectrophotometer. The formation of indophenol blue was determined using the absorbance at a wavelength of 655 nm. The concentration–absorbance curve was plotted using a series of standard ammonium sulfate ($(NH_4)(SO_4)_2$) solutions.

Product Analysis—^{15}N and ^{14}N Isotope-Labeling Experiment: To quantify the source of NH_4^+ in the nitrate reduction experiments, $Na^{14}NO_3/Na^{15}NO_3$ equal to 1:1 was used as the feeding N-source, and 0.5 M Na_2SO_4 was used as electrolyte. After 1 h electrolysis at −0.6 V (vs RHE), the obtained electrolyte containing $^{14}NH_4^+$-^{14}N and $^{15}NH_4^+$-^{15}N was taken out and adjusted to be weak acid (pH 6) with H_2SO_4, followed by adding 0.01 g maleic acid ($C_4H_4O_4$) as external standard. Then, 50 µL deuterium oxide (D_2O) was mixed with 0.5 mL of the above-mentioned solution for further quantification by 1H NMR. The calibration curves were created using a series of $^{4}NH_4^+$-^{14}N and $^{15}NH_4^+$-^{15}N solutions with known concentrations (50, 100, 150, 200, 250 ppm) as standards.

Product Analysis—In-Situ Differential Electrochemical Mass Spectrometry (DEMS) Measurements: In-situ DEMS measurements were constructed using a specially-made DEMS system, including an electrochemical workstation and a mass spectrometer, to identify the intermediates and products accurately. The three-electrode system and electrolyte were the same as the electrochemical measurements. To capture gas molecules in time, the sampling probe of the mass spectrometer was close to the working electrode with the coated catalyst. In a typical procedure, the vacuum system of the mass spectrometer was closed, and LSV scanning was conducted with a voltage range of 0–1.0 V at a sweep speed of 5 mV s^{-1} until the baseline was kept steady. Then, an open vacuum system of the mass spectrometer was used to capture gas molecules produced in the electrocatalytic process, and the corresponding mass signals were collected during four consecutive LSV scans.

Product Analysis—In-Situ Raman Spectroscopy: An in-situ Raman spectroscopy was performed using an electrochemical cell with a quartz window to test the objective. The MnFeCoNiCu HEA catalyst was used as the working electrode, immersing it into the electrolyte for sufficient ionic conductivity. Counter and reference electrodes were Pt wire and Ag/AgCl, respectively. The *i–t* measurements were conducted for 1 h electrolysis at −0.7 V (vs RHE). Meanwhile, the Raman spectra were collected every 6 min with a collection time of 20 s each.

Calculation of the Faradaic Efficiency and Yield Rate: The faradaic efficiency of NH_3 was calculated by the following Equation (2):

$$FE_{NH3}\,(\%) = \frac{8F \times c_{NH_3} \times V}{17 \times Q} \tag{2}$$

NH_3 yield rate was calculated by the following Equation (3):

$$\text{NH}_3\text{ yield rate } \left(\text{mg h}^{-1}\text{ cm}^{-2}\right) = \frac{c_{NH_3} \times V}{t \times s} \tag{3}$$

where F is Faraday constant (96 485 C mol^{-1}), c_{NH3} ($mg\ L^{-1}$) is the NH_3 concentrations after electrolysis at the reduction time t, V (mL) is the volume of the cathodic electrolyte, Q (C) is the overall charge passing the electrode, s is the geometric area of catalyst (cm^2).

Computational Details: The first principles of density functional theory (DFT) calculations were implemented in the Vienna ab initio Simulation Package (VASP).[50] All of the model structures were described by the Perdew–Burke–Ernzerhof (PBE) functional within generalized gradient approximation (GGA). The projector-augmented wave (PAW) method was implemented in plane waves with a kinetic energy cutoff of 500 eV to describe electron-ion interactions.[51] The Hubbard model (DFT + U) was used to describe the localized iron 3d electrons.[52] Using the conjugate gradient algorithm in the Large-scale Atomic/Molecular Massively Parallel Simulator (LAMMPS) platform, the atom coordinates are iteratively adjusted to create the disordered fcc structure of HEA. The terminated MnFeCoNiCu HEA slab model was constructed by cleavage of (111) surface according to the TEM results with the same atomic ratio of five metals. For geometry optimization, self-consistent, and the density of states (DOS) calculations, the k-point mesh was set to 3 × 3 × 1 in the first Brillouin zone. In the Z-direction, a vacuum layer of 15 Å was used for the MnFeCoNiCu HEA slab model to prevent the interaction between two adjacent layers. All calculations optimized the electronic iterations convergence until the energy was less than 10^{-5} eV and the Hellmann-Feynman forces were below 0.02 eV $Å^{-1}$. The density of states (DOS) and the electron localization function (ELF) were calculated using VESTA and VASPKIT.

The NO_3^- reduction process can be described as following Equations (4–12):

$$* + NO_3^- \rightarrow * NO_3 + e^- \tag{4}$$

$$* NO_3 + 2H^+ + e^- \rightarrow * NO_2 + H_2O \tag{5}$$

$$* NO_2 + 2H^+ + e^- \rightarrow * NO + H_2O \tag{6}$$

$$* NO + H^+ + e^- \rightarrow * NOH \tag{7}$$

$$* NOH + H^+ + e^- \rightarrow * NH_2O \tag{8}$$

$$* NH_2O + H^+ + e^- \rightarrow * NH_2OH \tag{9}$$

$$* NH_2OH + H^+ + e^- \rightarrow * NH_2 + H_2O \tag{10}$$

$$* NH_2 + H^+ + e^- \rightarrow * NH_3 \tag{11}$$

$$* NH_3 \rightarrow * + NH_3 \tag{12}$$

where * represents the active site. The reaction free energy change can be obtained as follows Equation (13):

$$\Delta G = \Delta E + \Delta E_{ZPE} - T\Delta S \tag{13}$$

where ΔE is the total energy difference between the reactant and the product, ΔE_{ZPE}, and ΔS are the changes in the zero-point energy and entropy obtained from the vibrational frequency calculations, respectively, and T is the temperature (T = 298.15 K).

To avoid obtaining the energy of charged NO_3^- species directly, the neutral HNO_3 gas phase was chosen to be a reference as below Equations (14) and (15):

$$HNO_3\,(g) \rightarrow HNO_3\,(l) \tag{14}$$

$$HNO_3\,(l) \rightarrow H^+ + NO_3^- \tag{15}$$

Hence, the Equation (6) can be rewritten as below Equation (16):

$$* + HNO_3 \rightarrow * NO_3 + H^+ + e^- \tag{16}$$

The Gibbs free energy of NO_3 ($\Delta G(^*NO_3)$) can be calculated as Equation (17):

$$\Delta G\,(NO_3 *) = G\,(* NO_3) - G\,(HNO_3) + \frac{1}{2}G\,(H_2) - G\,(*) + \Delta G\text{correct} \tag{17}$$

in which $G(^*NO_3)$, $G(HNO_3)$, and G (*) are the Gibbs free energy of adsorbed nitrate, vaporization of HNO_3 (l), and catalysts, respectively. $\Delta G_{correct}$ is the correction of adsorption energy.

Supporting Information

Supporting Information is available from the Wiley Online Library or from the author.

Acknowledgements

This work was financially supported by the City University of Hong Kong (project nos. 9229138, 9231502, and 9231539).

Conflict of Interest

The authors declare no conflict of interest.

Author Contributions

D.Y. conceived the idea and led the project. B.L., B.G., Y.M., and S.Z. processed the sample growth and structural characterization. M.C., D.C., C.Z., and Q.Q. processed the electrochemical measurements. D.Y. conducted DFT calculations. J.C.H. supervised the work. D.Y. wrote the manuscript. All authors made revisions and approved the manuscript.

Data Availability Statement

The data that support the findings of this study are available from the corresponding author upon reasonable request.

Keywords

electrochemical nitrate reduction, energy-scaling limitations, high-entropy alloy

Received: October 15, 2024
Revised: December 15, 2024
Published online:

[1] Y. Wang, C. Wang, M. Li, Y. Yu, B. Zhang, *Chem. Soc. Rev.* **2021**, *50*, 6720.
[2] P. H. van Langevelde, I. Katsounaros, M. T. Koper, *Joule* **2021**, *5*, 290.
[3] C. Fang, J. Zhou, L. Zhang, W. Wan, Y. Ding, X. Sun, *Nat. Commun.* **2023**, *14*, 4449.
[4] Q. Gao, B. Yao, H. S. Pillai, W. Zang, X. Han, Y. Liu, S.-W. Yu, Z. Yan, B. Min, S. Zhang, *Nat. Synth.* **2023**, *2*, 624.
[5] J. Pérez-Ramírez, N. López, *Nat. Catal.* **2019**, *2*, 971.
[6] R. Jia, Y. Wang, C. Wang, Y. Ling, Y. Yu, B. Zhang, *ACS Catal.* **2020**, *10*, 3533.
[7] Y. Wang, W. Zhou, R. Jia, Y. Yu, B. Zhang, *Angew. Chem., Int. Ed.* **2020**, *59*, 5350.
[8] T. Löffler, A. Ludwig, J. Rossmeisl, W. Schuhmann, *Angew. Chem., Int. Ed.* **2021**, *60*, 26894.
[9] S. Li, P. Ma, C. Gao, L. Liu, X. Wang, M. Shakouri, R. Chernikov, K. Wang, D. Liu, R. Ma, *Energy. Environ. Sci.* **2022**, *15*, 3004.
[10] W. Zhu, F. Yao, Q. Wu, Q. Jiang, J. Wang, Z. Wang, H. Liang, *Energy. Environ. Sci.* **2023**, *16*, 2483.
[11] Z. W. Chen, J. Li, P. Ou, J. E. Huang, Z. Wen, L. Chen, X. Yao, G. Cai, C. C. Yang, C. V. Singh, *Nat. Commun.* **2024**, *15*, 359.
[12] Y. Kang, O. Cretu, J. Kikkawa, K. Kimoto, H. Nara, A. S. Nugraha, H. Kawamoto, M. Eguchi, T. Liao, Z. Sun, *Nat. Commun.* **2023**, *14*, 4182.
[13] R. Zhang, Y. Zhang, B. Xiao, S. Zhang, Y. Wang, H. Cui, C. Li, Y. Hou, Y. Guo, T. Yang, *Angew. Chem., Int. Ed.* **2024**, *63*, 202407589.
[14] J.-T. Ren, L. Chen, H.-Y. Wang, Z.-Y. Yuan, *Chem. Soc. Rev.* **2023**, *52*, 8319.
[15] Y. Sun, S. Dai, *Sci. Adv.* **2021**, *7*, 1600.
[16] Y. Yao, Q. Dong, A. Brozena, J. Luo, J. Miao, M. Chi, C. Wang, I. G. Kevrekidis, Z. J. Ren, J. Greeley, *Science* **2022**, *376*, 6589.
[17] G. Feng, F. Ning, J. Song, H. Shang, K. Zhang, Z. Ding, P. Gao, W. Chu, D. Xia, *J. Am. Chem. Soc.* **2021**, *143*, 17117.
[18] J. Li, C. A. Triana, W. Wan, D. A. Saseendran, Y. Zhao, S. E. Balaghi, S. Heidari, G. Patzke, *Chem. Soc. Rev.* **2021**, *50*, 2444.
[19] S. Zhang, Y. Zha, Y. Ye, K. Li, Y. Lin, L. Zheng, G. Wang, Y. Zhang, H. Yin, T. Shi, *Nano Micro Lett.* **2024**, *16*, 9.
[20] J.-Y. Fang, Q.-Z. Zheng, Y.-Y. Lou, K.-M. Zhao, S.-N. Hu, G. Li, O. Akdim, X.-Y. Huang, S.-G. Sun, *Nat. Commun.* **2022**, *13*, 7899.
[21] J. Geng, S. Ji, H. Xu, C. Zhao, S. Zhang, H. Zhang, *Inorg. Chem. Front.* **2021**, *8*, 5209.
[22] R. Zhang, Y. Guo, S. Zhang, D. Chen, Y. Zhao, Z. Huang, L. Ma, P. Li, Q. Yang, G. Liang, *Adv. Energy. Mater.* **2022**, *12*, 2103872.
[23] M. Wang, S. Li, Y. Gu, W. Xu, H. Wang, J. Sun, S. Chen, Z. Tie, J.-L. Zuo, J. Ma, *J. Am. Chem. Soc.* **2024**, *143*, 8437.
[24] L. Gao, X. Li, Z. Yao, H. Bai, Y. Lu, C. Ma, S. Lu, Z. Peng, J. Yang, A. Pan, *J. Am. Chem. Soc.* **2019**, *141*, 18083.
[25] G. Lin, Q. Ju, X. Guo, W. Zhao, S. Adimi, J. Ye, Q. Bi, J. Wang, M. Yang, F. Huang, *Adv. Mater.* **2021**, *33*, 2007509.
[26] Y. Li, B. Wei, M. Zhu, J. Chen, Q. Jiang, B. Yang, Y. Hou, L. Lei, Z. Li, R. Zhang, *Adv. Mater.* **2021**, *33*, 2102212.
[27] S. Zhang, J. Wu, M. Zheng, X. Jin, Z. Shen, Z. Li, Y. Wang, Q. Wang, X. Wang, H. Wei, *Nat. Commun.* **2023**, *14*, 3634.
[28] M. Wei, Y. Sun, J. Zhang, F. Ai, S. Xi, J. Wang, *Energy Environ. Sci.* **2023**, *16*, 4009.
[29] Q. Gao, H. S. Pillai, Y. Huang, S. Liu, Q. Mu, X. Han, Z. Yan, H. Zhou, Q. He, H. Xin, *Nat. Commun.* **2022**, *13*, 2338.
[30] S. Sun, X. Zhou, B. Cong, W. Hong, G. Chen, *ACS Catal.* **2020**, *10*, 9086.
[31] X. Lei, Q. Tang, Y. Zheng, P. Kidkhunthod, X. Zhou, B. Ji, Y. Tang, *Nat. Sustainability.* **2023**, *6*, 816.
[32] J.-X. Liu, D. Richards, N. Singh, B. R. Goldsmith, *ACS Catal.* **2019**, *9*, 7052.
[33] W. J. Sun, H. Q. Ji, L. X. Li, H. Y. Zhang, Z. K. Wang, J. H. He, J. M. Lu, *Angew. Chem., Int. Ed.* **2021**, *60*, 22933.
[34] D. Chen, S. Zhang, D. Yin, W. Li, X. Bu, Q. Quan, Z. Lai, W. Wang, Y. Meng, C. Liu, *Adv. Energy. Mater.* **2023**, *13*, 2203201.
[35] Q. Song, M. Li, X. Hou, J. Li, Z. Dong, S. Zhang, L. Yang, X. Liu, *Appl. Catal., B* **2022**, *317*, 121721.
[36] M. Xie, S. Tang, Z. Li, M. Wang, Z. Jin, P. Li, X. Zhan, H. Zhou, G. Yu, *J. Am. Chem. Soc.* **2023**, *145*, 13957.
[37] S. Wang, H. S. Pillai, H. Xin, *Nat. Commun.* **2020**, *11*, 6132.
[38] H. Niu, Z. Zhang, X. Wang, X. Wan, C. Shao, Y. Guo, *Adv. Funct. Mater.* **2021**, *31*, 2008533.
[39] J. Gu, L. Li, Y. Xie, B. Chen, F. Tian, Y. Wang, J. Zhong, J. Shen, J. Lu, *Nat. Commun.* **2023**, *14*, 5389.
[40] Y. Men, D. Wu, Y. Hu, L. Li, P. Li, S. Jia, J. Wang, G. Cheng, S. Chen, W. Luo, *Angew. Chem., Int. Ed.* **2023**, *135*, 202217976.
[41] J. Hao, Z. Zhuang, K. Cao, G. Gao, C. Wang, F. Lai, S. Lu, P. Ma, W. Dong, T. Liu, *Nat. Commun.* **2022**, *13*, 2662.
[42] H. Li, Y. Han, H. Zhao, W. Qi, D. Zhang, Y. Yu, W. Cai, S. Li, J. Lai, B. Huang, *Nat. Commun.* **2020**, *11*, 5437.
[43] H. Zhu, S. Sun, J. Hao, Z. Zhuang, S. Zhang, T. Wang, Q. Kang, S. Lu, X. Wang, F. Lai, *Energy. Environ. Sci.* **2023**, *16*, 619.
[44] Q. Hu, Y. Qin, X. Wang, H. Zheng, K. Gao, H. Yang, P. Zhang, M. Shao, C. He, *CCS Chem.* **2022**, *4*, 2053.

[45] H. Yang, C. Wang, Y. Zhang, Q. Wang, *Sci. China Mater.* **2019**, *62*, 681.
[46] F.-Y. Chen, Z.-Y. Wu, S. Gupta, D. J. Rivera, S. V. Lambeets, S. Pecaut, J. Y. T. Kim, P. Zhu, Y. Z. Finfrock, D. M. Meira, *Nat. Nanotechnol.* **2022**, *17*, 759.
[47] J. Dai, Y. Tong, L. Zhao, Z. Hu, C.-T. Chen, C.-Y. Kuo, G. Zhan, J. Wang, X. Zou, Q. Zheng, *Nat. Commun.* **2024**, *15*, 88.
[48] K. Wang, R. Mao, R. Liu, J. Zhang, H. Zhao, W. Ran, X. Zhao, *Nat. Water.* **2023**, *1*, 1068.
[49] F.-Y. Chen, A. Elgazzar, S. Pecaut, C. Qiu, Y. Feng, S. Ashokkumar, Z. Yu, C. Sellers, S. Hao, P. Zhu, *Nat. Catal.* **2024**, *7*, 1032.
[50] G. Kresse, J. Hafner, *Phys. Rev. B* **1993**, *48*, 13115.
[51] J. Wellendorff, K. T. Lundgaard, A. Møgelhøj, V. Petzold, D. D. Landis, J. K. Nørskov, T. Bligaard, K. W. Jacobsen, *Phys. Rev. B—Condens. Matter. Mater. Phys.* **2012**, *85*, 235149.
[52] B. Himmetoglu, A. Floris, S. De Gironcoli, M. Cococcioni, *Int. J. Quantum Chem.* **2014**, *114*, 14.